aerospace

MDPI

Article

Experimental Aeroelastic Models Design and Wind Tunnel Testing for Correlation with New Theory

Deman Tang and Earl H. Dowell *

Department of Mechanical Engineering and Materials Science, Duke University, Box 90300, Hudson Hall, Durham, NC 27708-0300, USA; deman.tang@yahoo.com

* Correspondence: dowell@ee.duke.edu; Tel.: +1-919-660-5302; Fax: +1-919-660-0089

Academic Editor: Raffaello Mariani

Received: 25 January 2016; Accepted: 30 March 2016; Published: 14 April 2016

Abstract: Several examples of experimental model designs, wind tunnel tests and correlation with new theory are presented in this paper. The goal is not only to evaluate a new theory, new computational method or new aeroelastic phonomenon, but also to provide new insights into nonlinear aeroelastic phenomena, flutter, limit cycle oscillation (LCO) and gust response.

Keywords: flutter; limit cycle oscillation; freeplay nonlinearity; frequency lock-in; aeroelastic model

1. Introduction

A very important function of wind tunnel models and testing is to verify a new aeroelastic theory or a new computational method. For this purpose, experimental aeroelastic model design and manufacturing of scaled models, model ground vibration test and wind tunnel testing are essential to success. In the past 20 years, the Duke aeroelastic group has designed many aeroelastic models and conducted wind tunnel tests to evaluate new theoretical aeroelastic theories and new computations methods. They include:

(1) A high aspect ratio wing model. Several correlation studies for flutter and limit cycle oscillation (LCO) [1], limit cycle hysteresis response [2], gust response for clamped and flexibly suspended models [3,4] and Flutter/LCO suppression [5] were performed.

(2) Wing like plate models, delta wing-store, flapping flag, yawed plate and folding wing. The wing tunnel tests were used to evaluate the von Karman nonlinear plate theory, and a new nonlinear inextensible beam and plate theory and also some high fidelity computation methods. Based on these models several correlation studies for flutter/LCO [6–16] and gust response studies [17–19] were performed.

(3) Airfoil section with control surface freeplay. The wing tunnel tests were used to evaluate new approaches for the freeplay nonlinear and gust responses including Duke computational codes using the Peter's finite state airload aerodynamic theory, harmonic balance method, and the time marching integration based on state space equations [20–24] and the ZAERO code [25] based on the computational fluid dynamic (CFD) theory conducted by ZONA Technology, Inc.

(4) All-movable tail with freeplay model at the root [26,27] to similar horizontal tail in the actuating mechanism freeplay nonlinearity of aircraft. Based on this model a computational code has been developed and evaluated.

(5) A free-to-roll fuselage flutter model [28]. From measured wind tunnel data, one evaluates the predicted symmetric and anti-symmetric flutter/LCO theory.

(6) An experimental oscillating airfoil model at high angles of attack for measuring aerodynamic response. A frequency "Lock-in" phenomenon is found in buffeting flow and compared to the theoretical results [29]. Also, an experimental airfoil model with a portial-span control surface is conducted to measure the flap response of the portial-span induced by the buffeting flow [30].

Several examples of model designs, wind tunnel tests and experimental/theoretical correlation studies with the theory are presented in this paper. The goal is not only to evaluate a new theory, new computational method or new aeroelactic phonomenon, but also to provide new insights into nonlinear aeroelastic phenomena, flutter/LCO and gust response.

2. Experimental Models for Measuring Flutter/Limit Cycle Oscillation (LCO) Response to Evaluate a Nonlinear Structural Theory

Theoretical and experimental correlation study for the aeroelastic stability and response of an aircraft with a high-aspect-ratio wing and low-aspect-ratio wing have been studied for many years from subsonic to supersonic flow. Most investigators have used linear beam and plate theories to simplify the wing structural model. However, a geometric structural nonlinearity may arise from the coupling between elastic flap or vertical bending, chordwise or edgewise bending and torsion for very high aspect ratio wings typical of Uninhabited Air Vehicles (UAV) and also for the low aspect ratio wings. Here, two kinds of experimental wing models, a high altitude long endurance (HALE) model and a wing-like (plate) model are considered to evaluate the new nonlinear structural theories.

2.1. High Altitude Long Endurance Models (Nonlinear Beam Structural Theory and ONERA Aerodynamic Model)

An experimental high-aspect ratio wing aeroelastic model with a tip mass has been constructed and a wind tunnel test conducted to measure the static aeroelastic response, flutter and limit cycle oscillations. The goal is to assess experimentally the theoretical results using nonlinear structural and aerodynamic theories. The theoretical structural equations of motion are based on nonlinear beam theory by Hodges and Dowell [31] and the ONERA aerodynamic stall model [32].

The experimental model includes two parts: a high-aspect ratio wing with a slender body at the tip, and a root support mechanism. The wing is rectangular, untwisted and flexible in the flap, lag and torsional directions. The wing is constructed from a precision ground flat steel spar with mass uniformly distributed along the wing span. The spar is 45.72 cm in length, 1.27 cm in width and 0.127 cm in thickness. It is inserted tightly into the wing root mechanism. In order to reduce torsional stiffness, the spar has multiple thin flanges along the span. The flange width is 0.127 cm and it is 0.318 cm in deep. There are 2×33 flanges uniformly and symmetrically distributed along the wing span and center line of the spar. There are 18 pieces of NACA 0012 airfoil plate uniformly distributed along the span. The pieces of the airfoil plate are made of aluminum alloy with 0.254 cm thickness. A precision aerodynamic contour of the wing model is obtained. Each airfoil plate has a slot 1.27 cm in width and 0.127 cm in thickness at the symmetry line. The spar is inserted through these airfoil plate slots and they are permanently bonded together. Each space between two airfoil plates is filled with a light wood (bass) covering the entire chord and span which provides the aerodynamic contour of the wing. This wood provides a slight additional mass and a small addition to the bending and torsion stiffness.

A slender body is attached to the elastic axis of the wing tip. The slender body is an aluminum bar, 0.95 cm in diameter and 10.16 cm in length. A paraboloidal forebody and an aftbody with 1.14 cm length are fixed to two ends of the bar. The forebody and aftbody are made of brass.

The slender body is symmetrical and is designed to provide enough torsional inertia to reduce the natural torsional frequency sufficiently to induce flutter in the velocity range of the wind tunnel.

The root support mechanism is a socket that allows a change of the steady angle of attack at the root. The root socket is mounted to the mid point of side-wall of the wind tunnel

Figure 1a shows a photograph of the aeroelastic wing model in the wind tunnel.

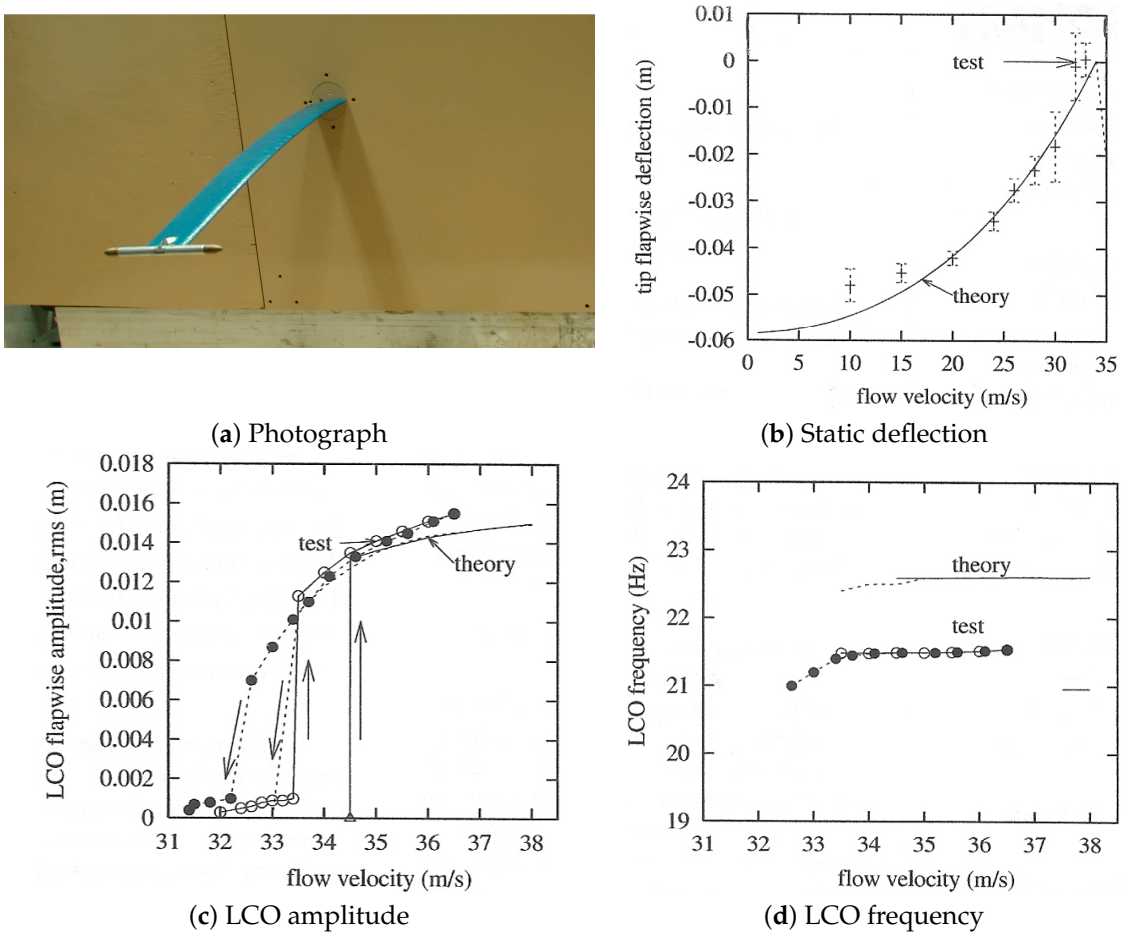

Figure 1. High altitude long endurance (HALE) experimental model and correlation analyses; (**a**) Photograph of model; (**b**) Static aeroelastic deflections at the wing tip; (**c**) Limit cycle oscillation (LCO) amplitude; (**d**) LCO frequency *vs.* flow velocity for pitch angle of attack $\theta_0 = 1.0°$.

Axial strain gages for bending modes and a 45° oriented strain gage for torsional modes were glued to the root spar to measure the bending-torsional deflections of the wing. Signals from the strain gages were conditioned and amplified before their measurement through a gage conditioner and a low-pass filter. A micro-accelerometer is mounted at the mid-span of the wing. The output signals from these transducers are directly recorded on a computer with data-acquisition and analysis software, Lab-VIEW 5.1.

A Helium-Neon Laser with 0.8 mw randomly polarized and wavelength 633 (nm) is mounted on the top of the tunnel. The top of the tunnel is made of a glass plate with a thickness of 1.27 cm. A mirror, 1.27 cm in diameter, is fixed on the tip of the wing. A "mirror" deflection technique is used to determine the geometric twist angle and the vertical or flapwise bending slope at the wing tip.

All static, flutter and LCO response tests were performed in the Duke University low speed wind tunnel. The wind tunnel is a closed circuit tunnel with a test section of 0.7×0.53 m^2 and a length of 1.52 m. The maximum air speed attainable is 89.3 m/s.

The basic parameters of the experimental wing model were obtained from standard static and vibration tests and are listed in the Table 1.

Table 1. Experimental wing model data.

Wing Properties	
Span (L)	0.4508 m
Chord (c)	0.0508 m
Mass per unit length	0.2351 kg/m
Mom. Inertia (50% chord)	0.2056×10^{-4} kgm
Spanwise elastic axis	50% chord
Center of gravity	49% chord
Flap bending rigidity (EI_1)	0.4186 Nm^2
Chordwise bending rigidity (EI_2)	0.1844×10^2 Nm^2
Torsional rigidity (GJ)	0.9539 Nm^2
Flap structural modal damping (ξ_w)	0.02
Chordwise structural modal damping (ξ_v)	0.025
Torsional structural modal damping (ξ_ϕ)	0.031
Slender Body Properties	
Radius (R)	0.4762×10^{-2} m
Chord length (c_{SB})	0.1406 m
Mass (M)	0.0417 kg
Mom. Inertia (I_x)	0.9753×10^{-4} kgm^2
Mom. Inertia (I_y)	0.3783×10^{-5} kgm^2
Mom. Inertia (I_z)	0.9753×10^{-4} kgm^2

We use a "mirror" deflection technique to measure the tip static aeroelastic deflections of the wing. A point determined by a reflected light source is marked on a readout grid paper placed on the top of the wind tunnel when the wing is undeflected. The readout grid paper is calibrated in the tip flap and twist deflections before the test. The reflected light source point with wing deflection as marked on the readout paper is then determined as the flow velocity is varied.

Figure 1b shows the the theoretical and experimental results of the tip flapwise deflection for a steady angle of attack, $\theta_0 = 1^\circ$. The solid line indicates the theoretical results and the bar indicates the measured data. The experimental data appear have some scatter due to the turbulent aerodynamic noise, although the noise is small. A very high measurement sensitivity is obtained from the mirror technique. We use a bar in the figure to indicate the magnitude of the response uncertainty. As shown Figure 1b, the tip deflection increase with increasing flow velocity, but the tip deflection is alway negative until the flow velocity reaches 34.5 m/s. At that velocity the aerodynamic forces provide sufficient lift to overcome the effect of gravity. At U = 34.5 m/s, the system enters into the flutter instability range. The consequent LCO has a certain non-zero mean or temporal average and this is shown by a dashed line in Figure 1b. Also, with LCO, aerodynamic stall occurs and the lift coefficient C_l suddenly decreases. The measured data in Figure 1b are acquired before the onset of flutter and LCO. The experimental data fall near the theoretical curves in Figure 1b. In general, the agreement is good except for some points at U = 10.15 m/s. In the higher flow velocity range, the data fluctuation increases due to greater aerodynamic turbulence.

A typical LCO amplitude and LCO frequency *vs.* flow velocity for $\theta_0 = 1^\circ$ and at the mid span position are shown in Figure 1c,d, respectively. The theoretical and experimental amplitudes are taken as rms average values from a 50 second sampling interval. The symbols, ○ and ●, indicate the experimental results for increasing and decreasing flow velocity, respectively. The solid and broken lines (without symbols) indicate the theoretical results for increasing and decreasing flow velocity, respectively. The symbol, △, indicates the linear flutter velocity which is calculated from the perturbation eigenvalue solution. For the increasing flow velocity case, the theoretical limit cycle oscillation occurs when the flow velocity is larger than the perturbation flutter velocity and the amplitude jumps from almost rest to a larger value. Once the onset of LCO occurs, the amplitude increases smoothly with increasing the flow velocity. When $U > 38.6$ m/s, a numerical or possibly a physical divergence is found in the theoretical model. For the case of decreasing flow velocity, as

shown by the broken line, the LCO amplitude decreases, but does not exactly coincide with those for the increasing velocity case. Also, there is a jump in the LCO response at U = 33.5 m/s which is a distinctly lower velocity than that found for the increasing velocity case (*i.e.*, U = 34.5 m/s).

The present experimental and theoretical results provide new insights into nonlinear aeroelastic phenomena of LCO beyond the linear flutter velocity for high aspect ratio wings. Also, these results show the nonlinear equations and stall aerodynamic equations provided by Hodges and Dowell and ONERA, respectively, and provide useful and accurate results for HALE vehicles.

2.2. *Flapping Flag and Yawed Plate Models (Nonlinear Inextensible Beam and Plate Theory)*

There is a substantial literature on inextensible beam theory, but relatively little on inextensible plate theory. A notable exception is the work of J. G. Simmonds and colleagues [33–36] on inextensible plate theory. His approach is quite different from the present one and ultimately leads to a system of ordinary differential equations for the plate deformation for a one dimensional generator curve from which the entire plate deformation may then be deduced. In the present new inextensible theory of beam and plate deformation as described in [37], the formulation is based upon Hamilton's Principle in terms of a single unknown, *i.e.*, the beam or plate deformation normal to its surface. The present approach has some substantial computational advantages, but the work of Simmonds is certainly elegant and pioneering.

The interaction between a cantilevered elastic plate and a uniform axial flow is a canonical fluid-structure interaction problem. If the flow is oriented *parallel* to the clamped leading edge the system is described as a wing-like configuration. If the flow is oriented *normal* to the clamped edge then the system is referred to as flag-like. There is extensive research on the aeroelastic response of the wing-like configuration due to the similarities between the simple cantilevered beam and aircraft wings. The present study differs from the classic explorations of the swept wing due to the application of the clamped boundary condition. For a traditional swept wing configuration, the clamp is applied parallel to the flow, changing the shape of the structure for every angle (it is called the yaw angle, β, in the present paper). For the current study, the clamped edge is rotated with the structure. In this case the second classic fluid structure interaction problem for a clamped-free elastic plate will be considered, *i.e.*, the flag-like configuration.

References [12,13] focus on exploring the transition of the limit cycle oscillation (LCO) response from a small yaw angle (flapping flag response for $\beta = 0$) to a large yaw angle (wing-like response, $\beta = 90°$) of a cantilever plate as the angle between the clamped edge and free stream velocity changes. In particular, [37] presents a nonlinear structural model for the rotated aeroelastic system. One creates the aeroelastic model by coupling this newly developed inextensible nonlinear plate structural model with a rotated vortex lattice aerodynamic model. The theoretical predictions were validated with aeroelastic experiments. Three distinct configurations, β = 0°, 45° and 90° were explored that show markedly different LCO transition behaviors.

Table 2 contains the material properties and geometry of the configuration. Table 3 shows the results of the ground vibration experiments in bending and torsion. The first column has the theoretical predictions using a ANSYS structural model with the parameters listed in Table 2. There is very good agreement between the theory (ANSYS code) and the experiment for all of the bending and torsion modes.

Table 2. Experimental plate properties.

ρ_s	E	h	L	C
2840 kg/m^3	70.6 $\times$ 10^9 N/m^2	0.381 mm	275 mm	151 mm

Table 3. Vibration test results.

Mode	ANSYS Code	Experiment	Error
	Freq (Hz)	Freq (Hz)	(Percent)
1st Bending	4.16	3.95	5.06
2nd Bending	25.84	24.98	3.3
3rd Bending	72.12	69.91	3.06
4th Bending	144.06	142.37	1.1
1st Twist	15.91	15.13	3.45
2nd Twist	45.73	49.05	7.16

The goal of the aeroelastic experiments was to quantify the LCO amplitude of the flapping flag ($\beta = 0^\circ$) as shown in Figure 2a. To capture the LCO amplitude, a Light Emitting Diode, LED, was placed at the tip and mid-span of the structure. Using 3D RPS video the path of the LED can be traced. Additionally the color coherence of the LED light, made it easier to use automated filtering in Matlab to track the path. To determine the amplitude of the oscillation, the code averages the snapshots from a full second of the video (30 frames) to get the average path. The script then automatically identifies the pixel of the far left and far right portion of the path and calls this the LCO amplitude. This amplitude is then synchronized with the wind tunnel velocity data to obtain the amplitude as a function of the velocity. The amplitude is converted to a real length using the camera calibration conducted before the experiment that calculates the pixels per centimeter in the plane of the LED. This method is able to provide the LCO amplitude to $+/-1$ centimeter. This could be improved by using a camera with a higher resolution. For the detail experimental measurement, see Reference [12].

The experimental data are presented as the measured nondimensional peak displacement from the panel tip. Figure 2b shows the nondimensional rms flap amplitude *vs.* the flow velocity. The theoretical results include two nonlinear cases: a full stiffness nonlinearity only and a full stiffness nonlinearity plus an inertia nonlinearity. The experimental results contain the LCO amplitude data for all of three different runs. The theoretical LCO responses are bursts or intermittent motion while the experimental results are primarily a single harmonic oscillation.

The experimental linear flutter speed can be estimated using an extrapolation method (this method is also used for other yaw angles), *i.e.*, an extrapolation of LCO response to zero amplitude. The experimental flutter speed is $U_f = 21.35$ m/s and the theoretical flutter speed is $U_f = 20.45$ m/s for $\beta = 0^\circ$.

It is interesting that the theoretical results for the full nonlinearities (inertia plus stiffness) agree best with experiment for the LCO amplitude. However, when only the stiffness nonlinearity is included, the response is a single dominant frequency, as found in the experiment.

For $\beta = 45^\circ$ and $\beta = 90^\circ$ yawed plates, to capture the LCO amplitude, a micro-accelerometer was placed at the trailing edge of these plate structures. Even though the micro-accelerometer is only 2.6 g, we include this weight in the computational model.

Figure 2c,d show the computational and experimental correlations of the LCO displacement response rms amplitude *vs.* the flow velocity for the yaw angle of $\beta = 45^\circ$. The correlation between the computations and experiments is reasonably good beyond the flutter speed. There are some smaller response amplitudes at lower flow velocities ($U < 15.75$ m/s) in the experiment. From the experimental curve of the LCO amplitude vs. the flow velocity, the experimental flutter speed is $U_f = 15.6$ m/s and the theoretical flutter speed is $U_f = 16.2$ m/s for $\beta = 45^\circ$.

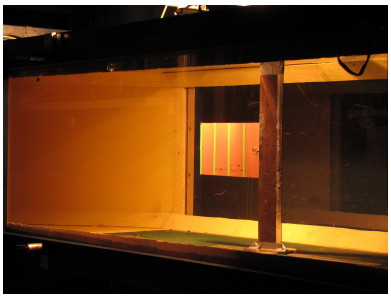

(a) $\beta = 0^0$

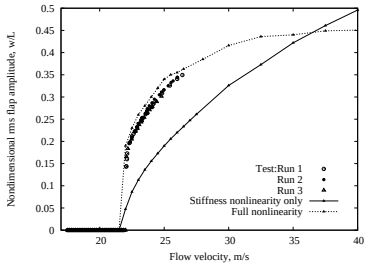

(b) **RMS amplitude**

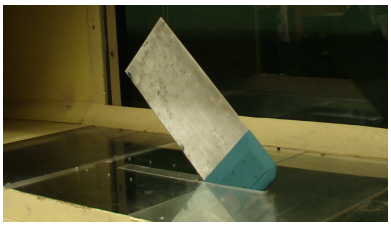

(c) $\beta = 45^0$

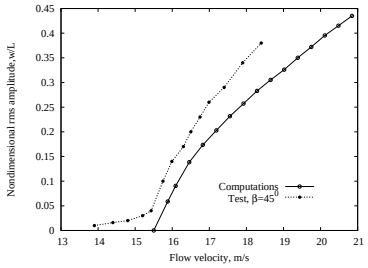

(d) **RMS amplitude**

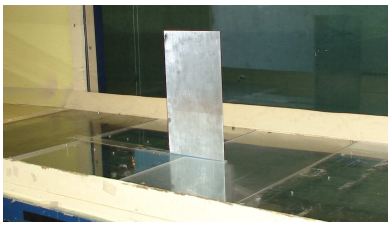

(e) $\beta = 90^0$

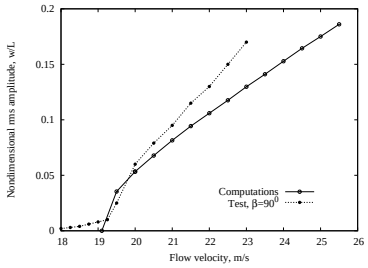

(f) **RMS amplitude**

Figure 2. Yawed plate models and correlation analyses; (**a**,**c**,**e**) for photographs and (**b**,**d**,**e**) for LCO rms amplitude versus the flow velocity for the yaw angle of $\beta = 0^\circ$, 45° and $\beta = 90^\circ$, respectively.

For $\beta = 90^\circ$, the plate is a wing-like. Figure 2e,f show the computational and experimental correlations of the LCO displacement response rms amplitude and corresponding LCO frequency versus the flow velocity for the yawed angle of $\beta = 90^\circ$. The correlation between the computations and experiments is fair beyond the flutter speed. There are some smaller response amplitudes at lower flow velocities ($U < 19$ m/s) in the experiment. The experimental flutter speed is $U_f = 19.3$ m/s and theoretical flutter speed is $U_f = 18.7$ m/s for $\beta = 90^\circ$.

By comparing computations and experiments for the LCO response of the several yawed plate configurations, it is shown that the present inextensible beam or plate theory as provided by Doewll and Tang [37] produces results in good agreement with the measured rms LCO amplitude. These theories have only a single unknown variable, *i.e.*, the transverse deflection of the beam or plate structure. This is very attractive for computations.

2.3. *Free-to Roll Fuselage Flutter Model (Symmetric and Anti-Symmetric Flutter/LCO Theory)*

A flutter model is often made using a semi-span wind-tunnel model with the root of the semi-span wing model clamped on the tunnel side wall. The experimental data obtained from such a model is suitable for computational aeroelasticity code validation. References [38–41] are studies

with typical subsonic and transonic flutter semi-span models. The boundary conditions of these experimental flutter modes are different from those of an actual aircraft, but the experimental data from the wind tunnel test may still be useful for offering the theory.

A fuselage which is free to roll is designed, but the vertical rigid body translation (plunge) and rotation (pitch) of the fuselage are constrained.The full span wing is a cropped delta wing plate for simplicity. The right and left wings are structurally symmetric. The full span wing dynamics are modeled using a linear plate wing structure theory. A three-dimensional time domain vortex lattice aerodynamic model is also used to investigate flutter of the linear aeroelastic system and results are correlated with experiment. See Reference [28] for more detail.

The experimental model consists of a right and left wing and a fuselage (slender body). For simplicity, the wing model is a cropped delta wing configuration which is constructed from a aluminum plate of thickness 0.0127 cm and has 40° leading edge sweep and 0° trailing edge sweep. The root chord is 12.7 cm and the halfspan length is 11.68 cm. The material properties of the wing are: mass density of 0.00284 kg/cm^2, Young's modulus of 720,000 kg/cm^2 and a Poisson's ratio of 0.3. The right and left wing model is assumed to be rigidly clamped along thefull root chord of the wing. The total rolling inertia about the fuselage center axis for the right and left wings is $J_w = 3.859 \times 10^{-5}$ kgm^2. A photograph of the aeroelastic model in the wind tunnel is shown in Figure 3a.

The fuselage has a circular cross-section with a diameter of 2.54 cm. It includes two parts. The front part is a slender body with a parabolic forebody which can rotate about the fuselage center axis and supports the wings. The rear part is a non-rotating slender body with a parabolic aftbody which is used to support the front portion of the slender body and is connected to the wind tunnel floor by a support or sting rod. The rolling inertia about the fuselage center axis for the rotating slender body is $J_f = 11.19 \times 10^{-5}$ kgm^2.

The wings are allowed to rotate (roll) about the center axis of the fuselage. The free or clamped mechanism for the rotation is provided by an electrical magnet brake that is used to provide rolling free or rolling clamped boundary conditions. Two strain gauges attached near the root of the two wings are used to measure the wing elastic deflections.

Because the experimental structural model has nonlinear behavior, the self-excited aeroelastic response represents a limit cycle oscillation (LCO) when the flow velocity is higher than the linear flutter speed. The linear critical flutter boundary is estimated from the LCO responses. The structural nonlinearity arises from a nonlinear strain-displacement relationship due to large structural deformations of the plate-like wings.

Figure 3b shows the measured rms LCO amplitude (microstrain) from the strain guage at the wing root *vs.* the flow velocity from U = 14 to 18 m/s for three cases. One is for the symmetric mode, *i.e.*, in the rolling fixed case. The other two cases are for the anti-symmetric mode with J_f/J_w = 2.9 and 13.5. The data are acquired when the response achieves a steady state limit cycle oscillation. The response is given by a rms value over the total sampling length. For the rolling fixed case, there are very small rms amplitudes from U = 14 to 17 m/s.It is believed that these responses are induced by the randomly fluctuating flow of the wind tunnel. At U = 17.1 m/s, the LCO rms amplitude jumps to a high amplitude response with a certain oscillating frequency. As the flow velocity continues to increase from U = 17.1 m/s, the LCO rms amplitude increases. An intersection between the extrapolated LCO amplitude curve and the flow velocity axis is defined as the linear critical flutter velocity. This estimated value is about U_f = 17.05 m/s. Similar to the symmetric mode case, for the anti-symmetric mode flutter at J_f/J_w = 2.9 and 13.5, the experimentally estimated linear critical flutter velocities are U_f = 16.6 and 16.7 m/s, respectively.

Figure 3c shows the theoretical and experimental (estimated) critical flutter boundary *vs.* J_f/J_w from J_f/J_w = 0 to 50. For the theoretical anti-symmetric mode flutter, the flutter velocity increases as J_f/J_w increases but the increase is small. For the theoretical symmetric mode flutter, the flutter boundary does not change with J_f/J_w as expected. When J_f/J_w becomes large, the linear flutter

velocity for the anti-symmetric mode approaches that for the symmetric mode. The experimental results for the anti-symmetric mode at J_f / J_w = 2.9, 13.5 and 38 are plotted in this figure as indicated by symbol of • and for the symmetric mode (rolling fixed case) is indicated by symbol of a black triangle. The maximum error is 3.5% for the flutter velocity. Figure 3d shows the corresponding flutter frequency. The maximum error is 3.5% for the flutter velocity and 7.5% for the flutter frequency.

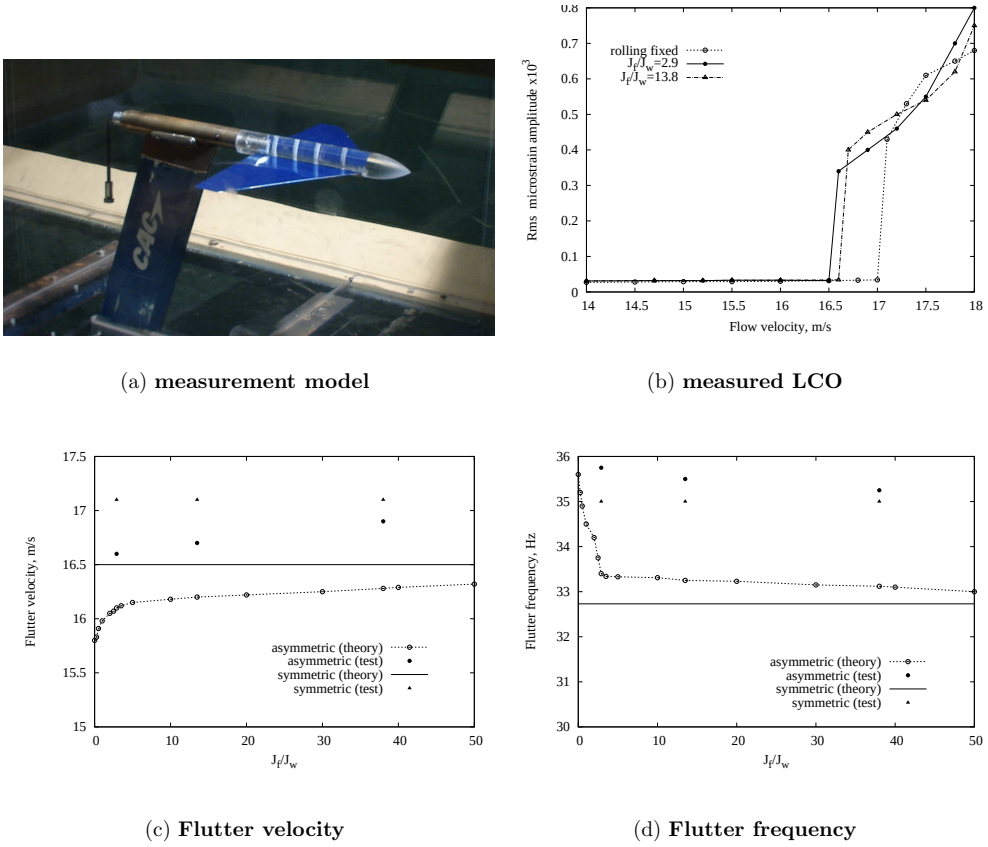

(a) **measurement model** (b) **measured LCO**

(c) **Flutter velocity** (d) **Flutter frequency**

Figure 3. Free-to-roll experimental model and correlation analyses; (**a**) Photograph of the model; (**b**) Measured LCO rms amplitude *vs.* flow velocity for symmetric mode (rolling fixed) and anti-symmetric mode at J_f / J_w = 2.9 and 13.5; (**c**) and (**d**) Flutter velocity and frequency *vs.* J_f / J_w.

The experimentally observed flutter mode is anti-symmetric, although theory suggests the symmetric mode flutter velocity is only modestly higher than that for the anti-symmetric modes. Correlation between theory and experiment for flutter velocity and frequency is good including the trends obtained when varying the ratio of fuselage to wing inertia.

3. Experimental Models for Measuring Flutter/LCO Response to Evaluate Nonlinear Freeplay Theory

The freeplay nonlinearity usually occurs in the following components of an aircraft: (a) between the main wing and the control surface actuating mechanism; (b) between the all-movable horizontal or vertical tail and the stabilizer or control actuating mechanism. In this section, two typical experimental models have been designed and constructed to simulate these freeplay nonlinearities: (1) an airfoil section with control surface freeplay and (2) all-movable tail with stabilizer freeplay.

3.1. Airfoil Section with Control Surface Freeplay

Early theoretical studies of aeroelastic systems with structural freeplay were carried out on analog computers by linearizing the system about the nonlinearity via describing functions or

harmonic balance or by time marching integration based on the state-space model. One of the compelling advantages of using harmonic balance or describing functions for aeroelastic systems is that traditional linear analytical tools, such as eigenanalysis, can be used for the determination of system stability while still allowing for the prediction of some nonlinear behavior. However, the response of a true nonlinear system may be dependent on the initial conditions, and the describing function approach does not permit a full exploration of this effect. The dependence on initial conditions and the wide variety of nonlinear behavior exhibited by systems with freeplay show the importance of incorporating this common physical nonlinearity into the theoretical model. In addition, the freeplay nonlinearity will likely have a significant effect on the response of the system to a control law designed for the nominal linear system.

In the present correlation study, a new nonlinear aerodynamic model, a finite state incompressible airloads model, developed by Peters [42] called "Duke code" and a ZAERO code based on CFD technology and nonlinear structural dynamics developed by ZONAT Trchnology, Inc. [25] have been used.

Experimental Model and Measurement System

The two-dimensional NACA 0012 rectangular wing model includes two parts: a main wing with a 19 cm chord and 52 cm span; and a flap with a 6.35 cm chord and 52 cm span, which is mounted at the trailing edge of the main wing using two pairs of micro-bearing with a pin. The main wing is constructed from an aluminum alloy circular spar beam with a diameter of 2.54 cm and a wall thickness of 0.32 cm. The beam runs through 14 pieces of NACA 0012 aluminum airfoil plate and serves as the pitch axis, located at the quarter-chord location from the leading edge. A 0.254 mm thick aluminum sheet covers the entire chord and span, providing the aerodynamic contour of the wing. In addition, an aluminum tube with 1.27 cm diameter is mounted from wing tip to wing tip at a location of 3.175 cm from the leading edge. The chordwise center of gravity can be adjusted by adding or subtracting a balance weight from this tube.

The flap is constructed in a similar manner with an aluminum alloy tube spar beam (1.27 cm diameter and 0.158 cm wall-thickness) passed through the leading edge of 14 pieces of NACA 0012 wood airfoil plate. The flap is also covered with the same type of aluminum sheet. Figure 4a shows the photograph of the experimental model including the ground vibration test.

A rotational axis comprised of the micro-bearings and pin allows the flap to have a rotational degree of freedom relative to the main wing. A steel leaf-spring is inserted tightly into a slot of the tube spar beam at one end of the flap. The free end of the leaf spring is inserted into a support block mounted on the main wing,see Figure 4b. The amount of structural stiffness that the leaf-spring provides can be adjusted by moving the support block toward or away from the rotational axis of the flap or by changing the diameter of the leaf-spring. Freeplay is incorporated by using a support block that allows the free end of the leaf-spring to move through a given range of motion before encountering resistance.

The support mechanisms for the entire model are mounted outside of the wind tunnel, at the top and bottom. The support mechanism at each end is a bi-cantilever beam made of two teel leaf-springs which are 20.32 cm long, 2.86 cm wide, and 0.102 cm thick. The distance between the two cantilever beams is 15.24 cm. A support block joins the free ends of the bi-cantilevered beams on both the top and the bottom and is free to move in the plunge direction. Figure 2 shows the plunging motion of the support structure. An identical structure is located on the bottom side of the wind tunnel. The two support blocks are the only parts of the support mechanism that move with the model, and this motion is restricted to the plunge degree of freedom. The pitch axis of the main wing is mounted to the upper and lower support blocks through a pair of precision bearings which have small amount of dry friction in the ball. This design allows the model to have a plunge motion that is independent of the pitch degree of freedom. At the upper bracket, there is a spring wire inserted tightly into the pitch axis of the wing. The ends of the spring wire are simply supported on the bracket, which

provides an adjustable pitch stiffness. The bracket is mounted on the upper support mechanism by three screws. The bracket allows rotation around the pitch axis when the screws are used to adjust the initial pitch angle.

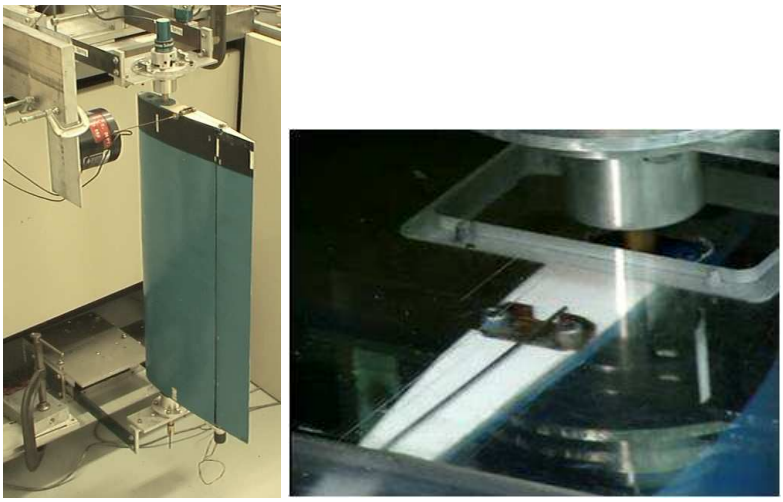

(a) **Experimental model** (b) **Photograph of flap bottom**

Figure 4. F Photograph of the experimental model (**a**) and photograph of freeplay mechanism (**b**).

The pitch angle of the main wing is measured by a rotational velocity displacement transducer, R30, which is fixed at the upper end of the pitch axis. The angular displacement transducer was calibrated and showed excellent linear response characteristic and high sensitivity. The plunge displacement is measured using another R30 which determines the motion of the upper support block. The flap rotational motion relative to the main wing is measured by a micro-RVDT which is mounted on the flap axis outside of the main wing. These three measurement signals are independent of one another.

The output from these transducers is amplified and directly recorded by data acquisition system, LabView 8.0 version in the computer. The digitized response data can be graphically displayed either on-line or off-line as a time history, phase plane plot, FFT, PSD, or Poincare map. In order to make a comparison of the theoretical and experimental data, a measurement system calibration was completed before the wing tunnel test. The dynamic calibration coefficients were determined by a ground vibration test. The system parameters for the experimental model are shown in Table 4.

From the experimental ground vibration results, a comparison of the structural natural frequencies for the numerical and experimental systems is given in Table 5.

Correlation study for zero angle of attack, α_0 = 0°

For the flutter/LCO test, a freeplay gap, $2 \times \delta = 2 \times 2.12°$, to be used. A nondimensional rms amplitude normalized by the freeplay gap is introduced here for LCO amplitude. The pitch and flap motions are nondimensionalized by the freeplay gap, *i.e.*, by $2 \times \delta$. For the plunge motion, it is nondimensionalized by $2 \times \pi\delta$ b/180°.

When the freeplay gap is set zero, the measured flutter flow velocity is 26.5 m/s for zero initial angle of attack. Because in this flow velocity range the model motion is very large we use an external device to limit the plunge motion amplitude. The measured flutter frequency is about 6.25 Hz.

Figure 5 shows the nondimensional plunge, pitch, flap LCO amplitudes and LCO frequency *vs.* the flow velocity for the initial pitch angle, $\alpha_0 = 0$. The motion may be periodic or non-periodic or chaotic. Here we use rms amplitude to present the LCO motion *vs.* the flow velocity.

Table 4. Experimental plate properties.

Model Parameters:	
Chord	0.254 m
Span	0.52 m
Semi-chord (b)	0.127
Elastic axis (a) w/r/t (b)	-0.5
Hinge line (c) w/r/t (b)	0.5
Mass Parameters:	
Mass of wing	0.713 kg
Mass of aileron	0.18597 kg
Mass/length of wing-aileron	1.73 kg/m
Mass of support blocks	0.467×2 kg
Total mass per span, M_h	3.625 kg/m
Inertial Parameters:	
S_α (per apn)	0.0726 kg
S_β (per span)	0.00393 kg
I_α (per span)	0.0185 kgm
I_β (per span)	0.00025 kgm
Stiffness Parameters:	
K_α (per span)	46.88 kgm/s^2
K_β (per span)	2.586 kgm/s^2
K_h (per span)	2755.4 kg/ms^2
Damping Parameters:	
ζ_α (half-power)	0.0175
ζ_β (half-power)	0.032
ζ_h (half-power)	0.0033

Table 5. Model natural frequencies.

	Computational	**Experimental**	**% Difference**
ω_α(coupled)	8.32 Hz	8.45 Hz	1.6
ω_β(coupled)	17.64 Hz	17.37 Hz	1.5
ω_h(coupled)	4.37 Hz	4.45 Hz	1.83
U_F(m/s)	27.3	26.5	2.9
ω_F(Hz)	6.05	6.25	3.3

As shown Figure 5, when the flow velocity, U, is less than 4.67 m/s no LCO occurs either for the theory or the experiment. When U is between 4.67 and 13.26 m/s for the experiment and 4.55 and 14.1 m/s for the theory, the motion is dominated by the plunge degree of freedom and has an oscillation frequency of about 4.5 to 5 Hz for both the theory and experiment. When U is between 13.26 and 25.6 m/s for the experiment and 14.1 and 27.4 m/s for the theory, the motion is dominated by the flap degree of freedom and has an oscillation frequency of about 10–10.5 Hz for the experiment and 9–9.5 Hz for the theory. When U is greater than 25.6 m/s, the experimental LCO amplitude abruptly increases and the test is stopped to protect the model (this is called the catastrophic flutter velocity). This flow velocity is close to the experimental flutter velocity (26.5 m/s) of the linear structure without freeplay. However, the theoretical catastrophic flutter velocity is 27.4 m/s and is slightly higher than the theoretical linear flutter velocity (27.3 m/s). For comparison, the computational results using CFD code, ZAERO, provided by ZONA Technology, Inc., are also presented in this figure.

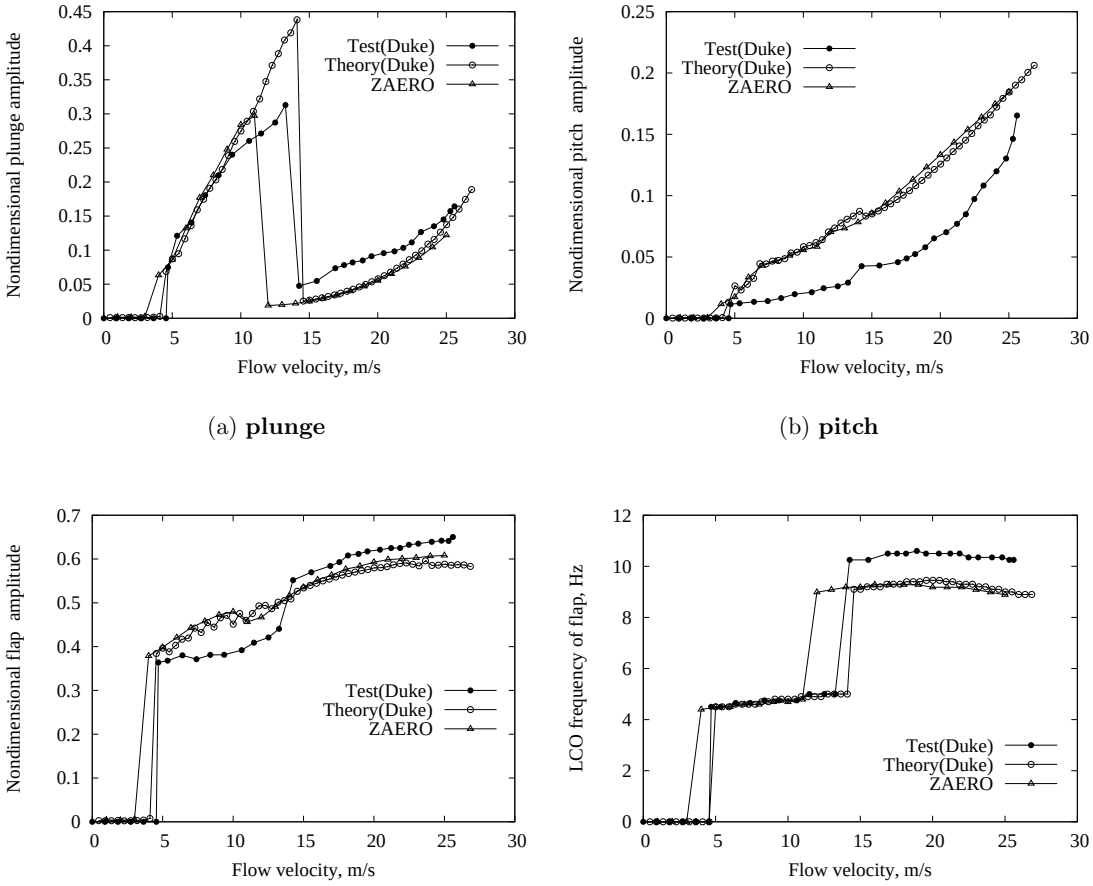

(a) **plunge** (b) **pitch**

(c) **flap** (d) **LCO frequency**

Figure 5. Theoretical and experimental LCO rms response amplitudes and frequency for the initial pitch angle of $\alpha_0 = 0$ and $\delta = 2.12°$.

Correlation study for no-zero angle of attack, $\alpha_0 \neq 0$

Experimental measurement for the several initial pitch angles of attack from $\alpha_0 = 2°$ to $8°$, are made to study the correlation. Here, only one case ($\alpha_0 = 6°$) is shown Figure 6. Summarizing the correlation results from $\alpha_0 = 2°$ to $\alpha_0 = 8°$, the following observations may be made.

(1) The flow velocity corresponding to a change in the LCO behavior from a lower frequency oscillation to a higher frequency oscillation changes modestly in the experiments as α_0 increases.

(2) The flow velocity corresponding to catastrophic flutter (very large LCO amplitude) also decreases as the initial pitch angle increases. The experimental results are 25.6 m/s for $\alpha_0 = 0°$; 25.05 m/s for $\alpha_0 = 2°$; 23.96 m/s for $\alpha_0 = 4°$; 21.48 m/s for $\alpha_0 = 6°$ and 20.43 m/s for $\alpha_0 = 8°$.

(3) When α_0 equals $8°$, the flow velocity range for the LCO becomes quite small and when α_0 is larger than $8°$ the LCO disappears both for the theory and test.

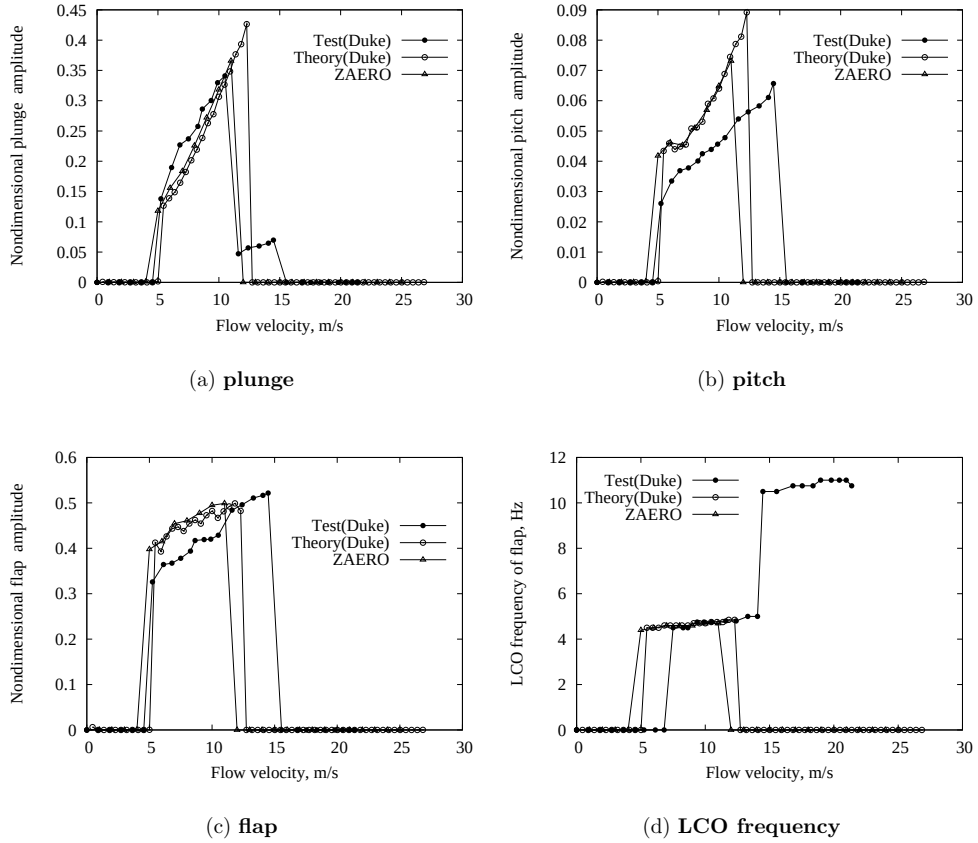

(a) **plunge** (b) **pitch**

(c) **flap** (d) **LCO frequency**

Figure 6. Theoretical and experimental LCO rms response amplitudes and frequency for the initial pitch angle of $\alpha_0 = 6^\circ$ and $\delta = 2.12^\circ$.

3.2. *All-Movable Tail Model with Freeplay*

Experimental models have been constructed by previous investigators that had free play nonlinearity in an all-movable tail in the actuating mechanism at the root, see References [43–45]. These early experiments were interpreted in terms of a reduction in flutter speed due to free play. However, the early works did not provide a LCO correlation analysis induced by the freeplay nonlinearity. Inspired by the early WADC (Wright Air Development Center) all-movable tail model, a similar experimental model was designed and tested. A computational code based on the linear three-dimensional time domain vortex lattice aerodynamic model and freeplay structural nonlinerarity has been developed to study the flutter and also nonlinear limit cycle oscillations (LCO) induced by a free play gap in the actuating mechanism at the root of the tail as well as the effects of the root rotation angle (nominal angle of attack) on LCO response. The tail model is mounted vertically in the wind tunnel. The effect of the gravity load is not considered in the computations and experiment discussed here although a later study included the effects of gravity by testing the model in a horizontal mount.

3.2.1. Experimental Model and Measurement System

A uniformly tapered wing from root to tip was designed to simulate a conventional unswept horizontal stalbilizer. The schematic of the all-movable horizontal tail model with free play gap in the root rotation mechanism is shown in Figure 7a. The experimental model includes two parts: a tapered wing and an actuating mechanism with torsional free play gap at the root. The tail wing is untwisted and flexible in the flap, lag and torsional directions. The root chord is 24.7 cm and tip chord is 13.2 cm and the span is 39.7 cm. The sweep angle of the lead edge is 5.7°.

The wing is constructed from a precision ground flat steel spar with mass uniformly distributed along the wing span. The spar is 39.7 cm in length, 1.905 cm in width and 0.127 cm in thickness. It is inserted tightly into the wing root mechanism. The spar elastic axis is located at 33 percent of the local chord aft of the leading edge which is consistent with the location for the axis of rotation of the tail, see Figure 7b.

There are 14 pieces of 2.6 cm wide sections uniformly attached to the spar along the span. Each section consists of a pair of ribs with NACA 0012 airfoil plate made of plastic material with 0.15 cm thickness. Each airfoil plate is fabricated using a Laser Printer and CAD software. Each airfoil section is constructed from two plastic airfoil plates and balsa wood. The wing is assembled by inserting the steel spar through a small slot cut through each of the sections. An additional 0.2 cm thick sheet of balsa wood is placed between each section and the wing is permanently bonded. The balsa wood placed between the airfoil sections provides some additional mass and stiffness in the bending and in torsion.

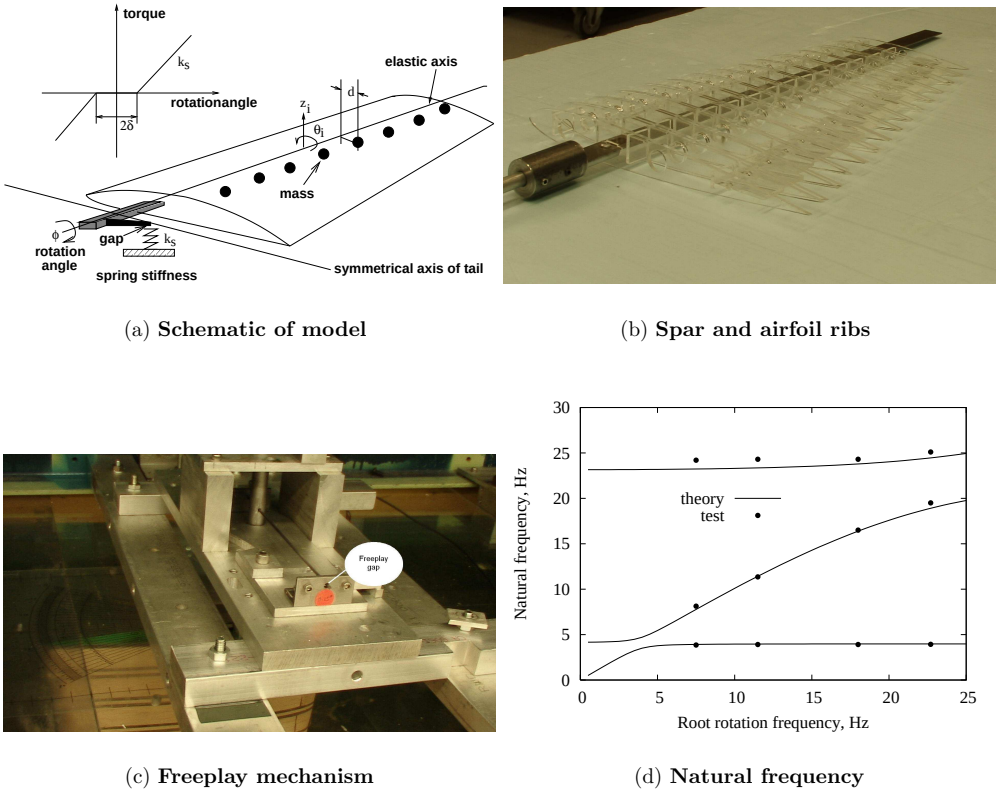

(a) **Schematic of model** (b) **Spar and airfoil ribs**

(c) **Freeplay mechanism** (d) **Natural frequency**

Figure 7. (**a**) Schematic of the all-movable tail model with free play in the root rotation mechanism; (**b**) and (**c**) Photographs of the model configuration and free play at root support mechanisms; (**d**) Natural frequency *vs.* uncoupled rotation frequency, ω_ϕ at the root.

The support mechanism for the entire tail model are mounted outside of the wind tunnel at the top. The wing spar axis is mounted to support blocks through a pair of precision bearings which have a small amount of dry friction in the ball, but this dry friction is not accounted in the computational code. There is a spring wire inserted tightly into a rotational axis between two bearings. The free end of the spring wire is simply supported on a bracket of the support block. The amount of rotational stiffness that the spring wire provides can be adjusted by moving the support block toward or away from the rotational axis of the wing. Each free play gap is incorporated by using a support block with a different size hole that allows the free end of the spring wire to move through a given range of motion before encountering resistance. A photograph of the spring wire assembly for the rotation stiffness (with free play) is shown in Figure 7c. The bracket is mounted on the support mechanism

by screws. The bracket allows rotation around the pitch axis when the screws are used to adjust the nominal pitch angle.

The root pitch angle of the wing is measured by a rotational velocity displacement transducer, R30, which is fixed at free end of the support block. The angular displacement transducer was calibrated and showed excellent linear response characteristic and high sensitivity. A 45° oriented strain gage for torsional modes were glued to the root spar to measure the torsional elastic deflections of the tail. Signals from the strain gages were conditioned and amplified before their measurement through a gage conditioner and a low-pass filter. A micro-accelerometer is mounted at the tip-span of the tail. The output signals from these transducers are directly recorded on a computer with data-acquisition and analysis software, Lab-VIEW 7.1.

A ground vibration test of the model was used to determine the natural frequencies and the modal damping. Figure 7d shows the theoretical and experimental natural frequencies at zero airspeed *vs.* the uncoupled rotation frequency, ω_ϕ. The first mode is dominated by the first bending and the second is dominated by the first torsion. The third mode is dominated by the second bending. When the tail wing is cantilevered, $\omega_\phi = \infty$, the first two theoretical bending frequencies are 3.99, 23.1 Hz and the first torsion frequency is 30.2 Hz. The experimental results are 4.0, 25.1 for bending and 27.75 Hz for torsion. In this case the agreement between the theory and experiment is good. Also it is found that the frequencies are close to the corresponding $\omega_\phi = \infty$ values (as shown in Figure 7d) over the higher ω_ϕ range. This means the coupling between the bending and torsion modes is weak.

3.2.2. LCO Correlation Study for $\alpha_0 = 0°$

Four typical free play gaps are selected. These are δ = 0.1°, 0.25°, 0.5° and 1°. The military specification (MIL-SPEC) confines the free play limit of all-moveable control surfaces to be less than 0.034° (peak to peak value) to achieve the goal of no free play induced LCO during normal operation of aircraft. In the present study, the maximum free play gap is limited to ± 1°. The uncoupled rotation frequency, ω_ϕ, is chosen to be 7.5 Hz, corresponding to root rotation stiffness, k_s = 2.895 Nm. Considering the effects of flight loads on tail free play induced LCO, the initial angles of attack vary from $\alpha_0 = 0°$ to 6°. The purpose of these computations is to determine the nominal angles of attack for which when the free play induced LCO disappears.

Depending on the initial conditions and physical parameters, the response may be either LCOs or chaotic oscillations, *i.e.*, the oscillation is generally around one of two equilibrium positions ($\pm\delta$), and the particular equilibrium position depends upon the initial conditions. Thus the oscillating displacement is essentially random with respect to time. In this study, we used a velocity response for the bending motion and a torsional rate for the torsional motion to present the LCO response behavior. A rms amplitude for the bending displacement velocity at the tail tip and a rms amplitude for the rotation angle at the root are calculated.

Figure 8a,b show the rms LCO amplitude of the bending velocity and at the tail tip (a) and the rms LCO amplitude of the root rotational angle motion (b) *vs.* the flow velocity for the initial disturbance angle, $+\delta$ at the root. The flow velocity range is from 0 to 22 m/s. Note that the linear flutter speed without free play is 23 m/s. In these figures results are included for four free play gaps, δ = 0.1°, 0.25°, 0.5° and 1°. From Figure 8, the following observations may be made.

(1) The theoretical LCO occurs over essentially the whole flow velocity range for which when $U > 0$. There is an oscillating divergence from the LCO motion when the flow velocity is greater than the linear flutter speed, *i.e.*, $U \geq U_f$. The experimental LCO occurs when flow velocity is larger than about 5 m/s. Below 5 m/s there is no measured LCO due to a dry friction torque in the root rotation mechanism. Without this dry friction torque, LCO is predicted to occur at even lower flow velocities.

(2) The rms amplitude for both the bending and torsional response increases as the flow velocity increases.

(3) The rms amplitude for the root rotational angle response oscillates around the gap region. The amplitude varies with the flow velocity which depends upon the initial conditions.

(4) As expected the rms amplitude for both the bending and torsional response increases as the free play gap increases.

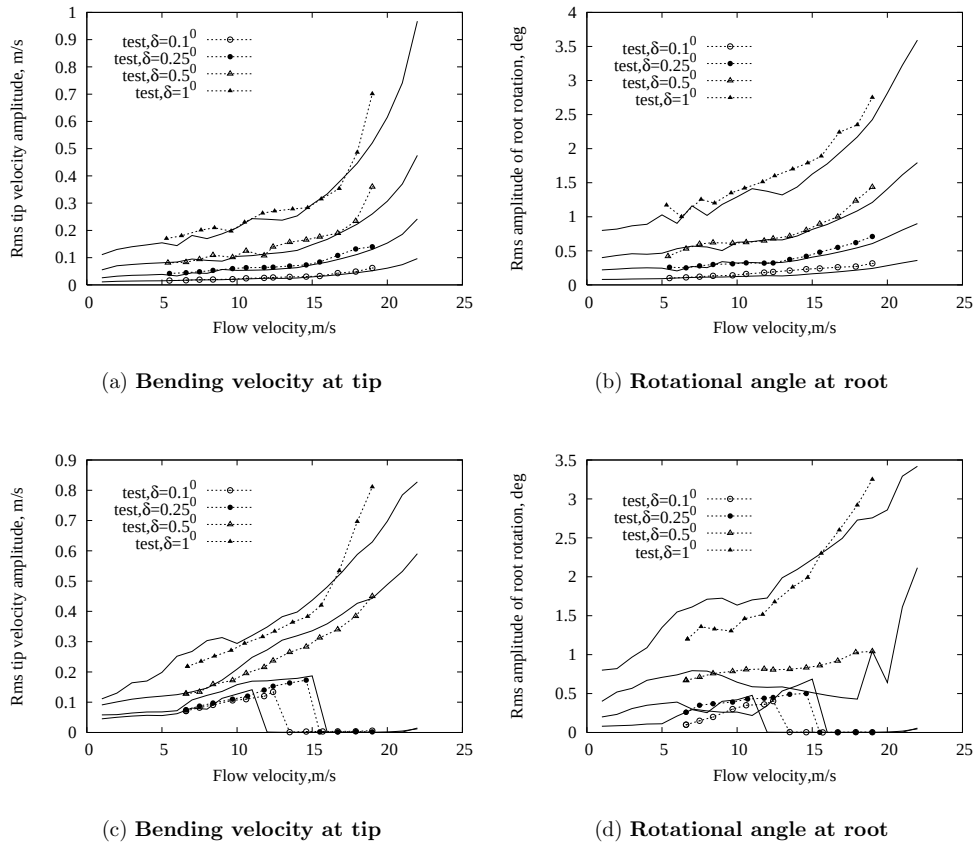

(a) **Bending velocity at tip** (b) **Rotational angle at root**

(c) **Bending velocity at tip** (d) **Rotational angle at root**

Figure 8. Correlation analyses for the all-movable model; (**a**) Tip bending velocity and (**b**) Root rotational angle *vs.* the flow velocity for $\alpha_0 = 0^\circ$ and (**c**,**d**) for $\alpha_0 = 2^\circ$.

3.2.3. LCO Correlation Study for $\alpha_0 \neq 0^\circ$

Five typical nominal angles of attack, $\alpha_0 = 1^\circ$, 2°, 4°, 6° and 8° and four free play gap values as described before. Only one case is presented here. Figure 8c,d show the rms LCO amplitude for a nominal angle of attack, $\alpha_0 = 2^\circ$. For two free play gaps, $\delta = 0.1^\circ$ and $\delta = 0.25^\circ$ LCO disappears above a certain flow velocity. The corresponding flow velocities for which LCO disappears, U_{no-LCO}, are 12 m/s for the theory and 13.5 for the test in the case of $\delta = 0.1^\circ$ and 16 m/s for the theory and 14.6 m/s for the test in the case of $\delta = 0.25^\circ$ respectively. When $\delta > 0.25^\circ$, LCO response occurs over the whole flow velocity range $U_f > U > 0$.

Summarizing the theoretical and experimental results for $\alpha_0 = 1^\circ$ to 8°, a disappearance of the LCO boundary is listed in Table 6. Note that the values in the parenthesis show the results from the tests. Also as the nominal angles of attack increases from 1° to 8°, the following observations may be made.

(1) The flow velocity for LCO disappearing increases when the angle of attack decreases for a given free play gap.

(2) The free play boundary for LCO disappearing increases when the angle of attack increases for a given flow velocity.

(3) As expected the LCO rms amplitude for both the bending and torsional responses increases with increased free play gaps. These results are similar to those for $\alpha_0 = 0^\circ$.

(4) Note that LCO also disappears for flow velocities less than about 6.5 m/s which is attributed again to the presence of friction in the root support mechanism.

Table 6. Flow Velocity at which LCO Disappeared, U_{no-LCO} m/s.

α_0/δ	**0.1°**	**0.25°**	**0.5°**	**1.0°**
1°	17/(15.7) m/s	None	None	None
2°	12/(13.5) m/s	16/(14.6) m/s	None	None
4°	8/(0) m/s	13/(11) m/s	16/(14.1)	None
6°	0/(0) m/s	10/(0) m/s	15/(13)	17/(14.7)
8°	0/(0) m/s	0/(0) m/s	13.5/(0)	15.5/(12)

The quantitative agreement between the theory and experiment is reasonably good for zero and non-zero angles of attack. The fair to good quantitative agreement between theory and experiment verifies that the present method has reasonable accuracy and good computational efficiency for the flutter/LCO analysis.

4. Experimental Models for Measuring Aerodynamic Response Phenomenon in Buffeting Flow

In earlier computational work by Raveh and Dowell, References [46,47], large shock oscillations (buffet oscillations) are observed for a certain combination of Mach number and steady mean angle of attack even in the absence of structural motion. Also in lower Reynolds number flow, bluff bodies in cross flow [48], and a flat plate at high angles of attack [49] are observed to have the nonlinear oscillations induced by the buffeting flow. In the buffeting flow there is a very interesting phenomenon called "frequency lock-in". Under certain flow conditions, the shedding frequency can lock into the natural frequency of the structure. In this Lock-in region, the structural response amplitude can reach a limit cycle oscillation that may cause high cycle fatigue and eventually failure.

Two experimental models were constructed to observe the buffeting flow oscillation. One is to find lock-in region by measuring the pressure variation on the oscillating airfoil surface at high angles of attack. Another is to construct a partial-span control surface (flap) attached to near the mid-span of a NACA0012 airfoil model with and without freeplay gaps at high angle of attack and to measure the flap response induced by the buffeting flow.

4.1. An Oscillating Airfoil Section Model in Buffeting Flow

4.1.1. Experimental Model and Measurement System

In order to observe the dynamic and static pressure distribution and measure the aerodynamic loading due to a high nominal angle of attack and a small pitching oscillation through wind tunnel tests, a typical section wing model was constructed. Design of the typical section took into account the fact that it must accommodate a root pitching oscillation, mount 20 micro-pressure sensors, PCB model 103B01, for dynamic pressure measurement and 20 orifices for the static pressure taps at the mid-span and also be mounted in the Duke University wind tunnel using an existing pitch oscillating testing rig.

The profile of the typical section is a NACA 0012 symmetrical airfoil, having a chord length of 0.2554 m, which nicely accommodates 20 dynamic pressure sensors and 20 static pressure taps. The span, l = 0.52 m of the typical section was dictated by the height of the wind tunnel, as the typical section is to be mounted vertically. Eight pieces of NACA0012 airfoil ribs made of aluminum material with 0.64 cm thickness are used for high chordwise stiffness and for adequate housing for bearings supporting the small strip hinge. In addition, a mid-span aluminum rib with 1.27 cm thickness provides support for 20 pressure sensors, see Figure 9a. The airfoil ribs are placed on three spars that, in addition to being structural elements, have specific functional roles.The spar placed at the quarter chord is an aluminum tube and serves to mount the model on the testing rig that is connected to a pitch oscillating testing rig to create an airfoil pitch oscillation.

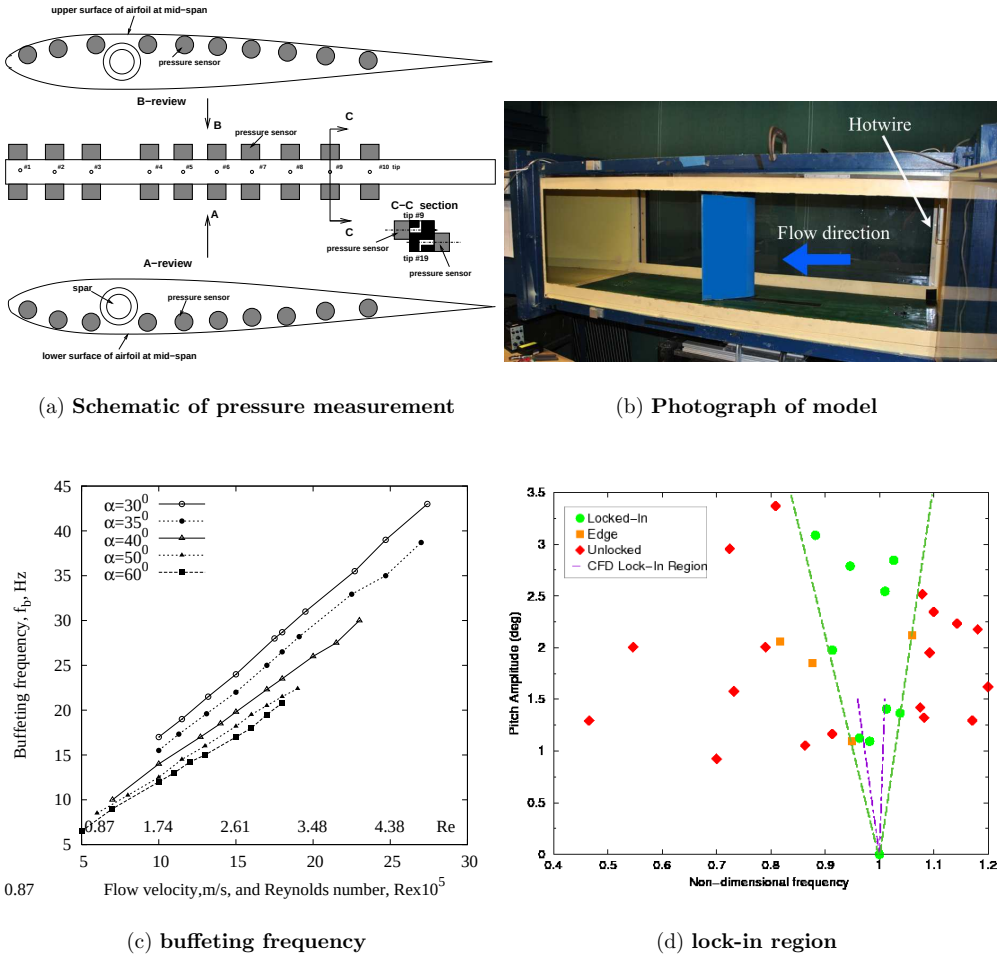

(a) **Schematic of pressure measurement** (b) **Photograph of model**

(c) **buffeting frequency** (d) **lock-in region**

Figure 9. Oscillating airfoil model in the buffeting flow and correlation analyses; (**a**) Schematic of pressure measurement; (**b**) Experimental model in wind tunnel at high angles of attack; (**c**) Buffet frequency varies flow velocity and Reynolds number, Re, for "onset" boundary of the buffet flow for nominal angles of attack, α = 30° to 60°, (**d**) Experimental and theoretical lock-in region for α = 40° and the Reynolds number, R_e = 100,000 (U = 5.8 m/s).

The mid-span airfoil rib is specially made to measure the dynamic pressure distribution at mid-span and provide support for the 20 micro-pressure sensors. There are 20 orifices of 1.16 mm diameter for the pressure taps which are symmetrically distributed over the upper and lower surfaces, respectively. The orifice positions in terms of percentage chord from the leading edge are 0.06, 0.12, 0.18, 0.3, 0.42, 0.49, 0.54, 0.61 and 0.74. The pressure sensor is bolted on the mid-span airfoil rib and installed with an adhesive mounting ring to prevent a pressure leak between the pressure surface of the sensor and the airfoil orifice. The dimensions of the pressure sensor are 9.5 mm diameter, 7 mm height. The weight is 3.26 g. The signal/noise is 60 db, *i.e.*, the uncertainty is 0.1%. Th dynamic range is 77 db and the frequency range is 5 Hz to 13 kHz. Details of the dynamic pressure measurement device are shown in Figure 9a. All the structural elements are held together by epoxy resin and mechanical elements (bolts, pins, *etc.*). They are covered with 0.25 mm in thick aluminum foil (called skin).

The root airfoil pitch excitation was performed by a pitch oscillatory shake table which is mounted to a very heavy support frame that is attached to the ground. The shake table is driven using a DC servo motor through a cam.The driving frequency is controlled by a D/A NB-MIO-16 system. A nearly pure single harmonic excitation is provided. A photograph of the wind tunnel model and the pressure measurement system in the model is shown in Figure 9b.

For the dynamic pressure measurement, the output of each pressure sensor and pitch oscillating displacement was directly recorded on a PC computer through signal conditioners, PCB models481A02, 442C04 and a data acquisition package which consisted of a 20-channel analog to digital (A/D) plug-in interface board, a BNC termination box,and data acquisition and analysis software, LabVIEW version 9.0.

4.1.2. Correlation Analyses for Frequency Lock-in Region

In this section, for comparison with the experimental results, the computational fluid dynamic analyses of NACA0012 are conducted using a nonlinear, frequency domain, harmonic balance (HB) code [50]. The viscous, Reynolds-averaged Navier-Stokes equations are solved for a 2D slice using a Spalart-Allmaras turbulence model. The O-grid contains 385 points in the circumferential direction, 97 points in the radial direction and extent approximately 20 diameters from the airfoil.

Aerodynamic response at buffet flow conditions with no pitch excitation were measured for different flow velocities from U = 5 to 27.5 m/s and several nominal angles of attack, α = 30° to 60°. The results are shown in Figure 9c in a plot of buffeting frequency *vs.* flow velocity and corresponding Reynolds number for the "onset" boundary of the buffet flow.

For aerodynamic response to pitch excition in the buffeting flow, a pitch sinusoidal excitation at the airfoil root is added. The pitch excitation amplitudes, θ_0, are considered in the present experiment from θ_0 = 0.8° to 3.4°. The excitation frequency, f_e ($\omega_e = 2\pi f_e$) varies from 5 to 12.5 Hz for the nominal angle of attack, α = 40° and the flow velocity, U = 5.8 m/s and Reynolds number R_e = 100,000.

Figure 9d shows the experimental lock-in region found by enforcing the airfoil oscillations at a fixed amplitude and frequency. The non-dimensionalized frequency is defined as f_e/f_b. The angle of attack is 40° and the Reynolds number is 100,000 (U = 5.8 m/s). Figure 9d and other comparable data may be found in Besem *et al.* [51]. The diamond symbols represent conditions where the shedding and enforced frequencies are unlocked, the circle symbols show lockin conditions, and the square symbols have a chaotic behavior that can be attributed to the edge of the lock-in region. The "V" shape is similar to the numerical results conducted by HB code [50], though the lock-in region is narrower numerically, which can be attributed to the chaotic behavior on the edges of the lock-in region. In the experiments, it is difficult to separate the frequencies due to the motion and due to the shedding because of the noise in the measurements. However, the computational code solution will only converge if the two frequencies are perfectly locked-in. This explains why the edges of the lock-in region are difficult to compare with the experiments.

From Figure 9c,d the following observations may be made.

(1) The buffeting frequency is almost directly proportional to the flow velocity or Reynolds number for any nominal angle of attack.

(2) The buffeting frequency (the starting points of the curves) depends on a combination of nominal angle of attack and flow velocity or Reynolds number.

(3) As the nominal angle of attack increases the buffeting frequency decreases for a certain flow velocity or Reynolds number.

4.2. An Airfoil with and without Freeplay Control Surface in Buffeting Flow

4.2.1. Experimental Model and Measurement System

The airfoil experimental model and the pressure measurement system are the same as described above. This model is mounted vertically to a very heavy support frame that allows one to adjust the nominal angle of attck of this model. The rotation center is at the one quarter chord of the airfoil. A photograph of the experimental model is shown in Figure 10a.

Based on the above model, a partial span control surface (flap) with 5.08 cm chord and 5.08 cm span is mounted on the wing model at span location, y = 28 cm and chord location of

x = 20 cm. The flap pitch rotation axis is placed at x = 20 cm. The rotation axis is comprised of two micro-bearings and allows the flap to have a rotational degree of freedom relative to the main wing. A steel leaf-spring is inserted tightly into a slot of the rotation axis of the flap. The free end of the leaf-spring is inserted into a support block mounted on the main wing. The amount of structural stiffness that the leaf-spring provides can be adjusted by moving the support block toward or away from the rotational axis. Freeplay is incorporated by using a support block that allows the free end of the leaf-spring to move through a given range of motion before encountering resistance. A schematic of the leaf spring assembly for the partial control surface (with freeplay) is shown in Figure 10b.

Two strain gauges are glued to both sides near the fixed end of the leaf-spring and are used to measure the flap pitch angle. The pitch angle calibration has been made from the strain gages. There is almost a linear relationship between the output voltage and the input pitch angle within 15 degrees. The average sensitive coefficient is 1.115 degree/voltage. For the dynamic pressure and flap pitch angle measurements , the output of each pressure sensor and pitch angle were directly recorded on a PC computer through signal conditioners and a data acquisition package which consisted of a 20-channel analog to digital (A/D) plug-in interface board, a BNC termination box, and data acquisition and analysis software, LabVIEW version 9.0.

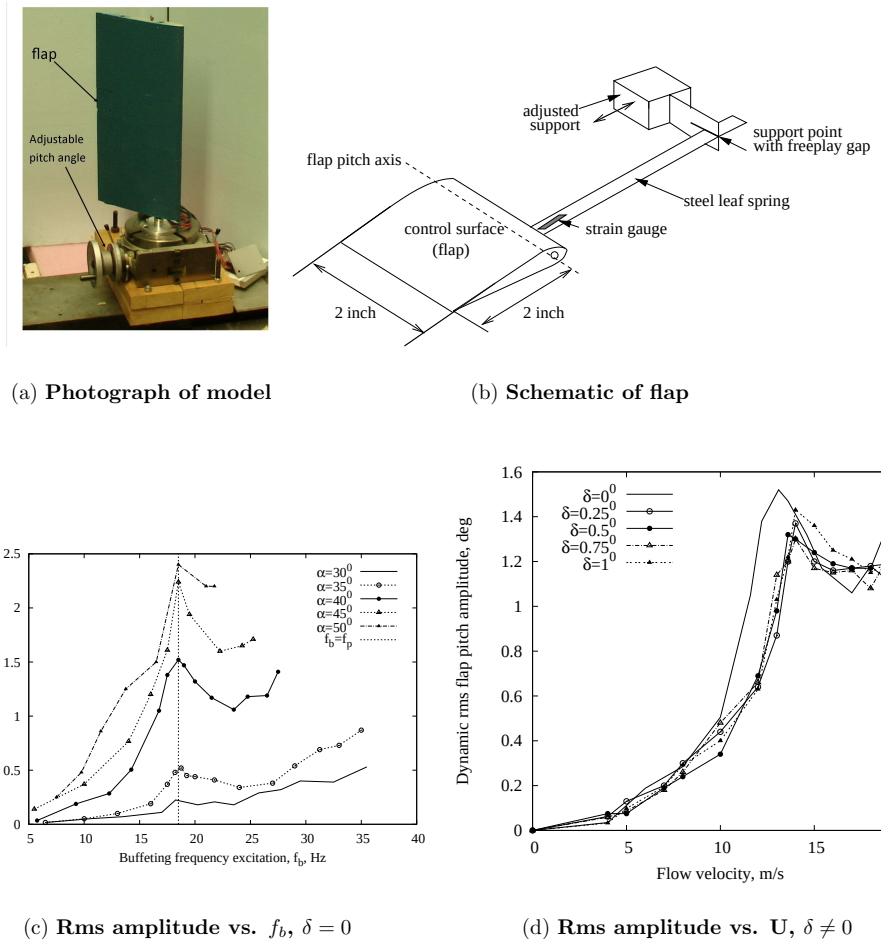

(a) **Photograph of model** (b) **Schematic of flap**

(c) **Rms amplitude vs.** f_b, $\delta = 0$ (d) **Rms amplitude vs. U,** $\delta \neq 0$

Figure 10. Experimental Freeplay model and correlation analyses in buffet flow; (**a**) Photograph of model; (**b**) Schematic of a portion of main wing-partial span surface assembly; (**c**) Dynamic rms flap pitch amplitude *vs.* buffet frequency for α = 30° to 50° without freeplay; (**d**) Dynamic rms flap pitch amplitude *vs.* flow velocity for α = 40° and freeplay gap, δ = 0.25° to 1.0°.

Because of unavoidable freestream and boundary layer turbulence irregularities, the free stream turbulence levels are about 1% of the nominal velocity. In order to remove this randomness from

the pressure data, an ensemble averaging procedure over a total of 20 records was carried out. The response is given by a rms value over the total sampling length for the experimental data. For the FFT analysis of these experimental data, an ensemble averaged FFT analysis has been used. Twenty (20) test time samples are taken to do the FFT analysis and an averaged FFT amplitude and frequency are determined.

4.2.2. Measured Aeroelastic Response of the Flap Induced by Buffeting Flow

The experimental flap pitch stiffness is $k_p = 0.0569$ Nm/rad and the flap pitch moment of inertia is $J_p = 0.42155 \times 10^{-5}$ kgm^2 and the corresponding flap pitch natural frequency is $f_p = 18.25$ Hz. All aeroelastic flap response tests were performed for nominal angles of attack from $\alpha_0 = 30^\circ$ to 50° and the flow velocity varies from 5 m/s to 26 m/s. Four freeplay gap ranges are considered in the wind tunnel tests, $\delta = \pm\, 0.25^\circ, \pm\, 0.5^\circ, \pm\, 0.75^\circ$ and $\pm\, 1.0^\circ$.

Figure 10c shows flap rms pitch amplitude *vs.* the buffeting frequency, for the nominal angles of attack $\alpha_0 = 30^\circ$ to 50° without freeplay gap. There is a local peak amplitude for each nominal angle of attack. Corresponding to these peak amplitudes, the flap is excited by a larger aerodynamic load with a certain excitation frequency, *i.e.*, the buffet frequency, f_b. (Recall that the buffet frequency is given in Figure 9c as a function of flow velocity for the various angles of attack.) At the peak response values, the buffeting frequencies are close to the flap natural frequency, f_p. We use a dotted line to connect these peak points in this figure. The rms dynamic flap responses are created by two different types of flow separation: one is due to a randomly fluctuating flow as shown for $\alpha_0 < 28^\circ$ and the other is due to a von Karman street vortex flow that has a dominant frequency when $\alpha_0 > 30^\circ$. The fluctuating flow has a white noise characteristic and the noise strength increases as the flow velocity increases. This noise excitation always leads to an increase in rms flap amplitude with increased flow velocity, but the von Karman street vortex flow or buffeting flow significantly increases the rms flap amplitude when the buffeting frequency is close to the flap natural frequency.

Generally, the rms flap response amplitude increases as the nominal angle of attack increases. For example, when $\alpha_0 = 30^\circ$, the buffet flow strength, *i.e.*, the peak value at the buffeting frequency, is relatively weak. Indeed, for the range of $28^\circ < \alpha_0 < 30^\circ$ it is difficult to identify the dominant buffeting frequency from the measured flap response due to the weak buffeting flow. When $\alpha_0 > 40^\circ$ the buffet flow strength is stronger and the effect on the flap response is significant.

The dynamic rms amplitude of the flap pitch angle *vs.* the flow velocity for four freeplay gaps at nominal angle of attack, $\alpha_0 = 40^\circ$ is shown in Figure 10d. The dynamic rms amplitude does not increase monotonically with an increased flow velocity. There is a local peak amplitude for each freeplay gap. Corresponding to these peak amplitudes, the flap is excited by a larger aerodynamic load with a buffeting flow frequency, f_b and these buffeting frequencies are close to the flap natural frequency, f_p. Corresponding to the peak amplitude, the flow velocity, $U_{p-p} = 13.1$ m/s and frequency $f_b = 18.5$ Hz for no freeplay gap. The U_{p-p} values for different freeplay gaps are also very close to $U = 13.1$ m/s. The corresponding f_{p-p} values for different freeplay gaps are very close to the buffeting frequency, f_b. It is interesting to note that the peak rms amplitude for different freeplay gaps are also close to the value for no freeplay case. This means the effect of the freeplay gap on the dynamic response of the flap motion is small.

Due to the larger static preload of the aerodynamic forces, the flap pitch motion is always near to one side of the freeplay boundary. The flow buffeting frequency *vs.* the flow velocity can be determined from measured flap motion. The results show that the flow buffeting frequency is almost independent of the freeplay gaps, as expected.

The buffet flow occurs at large angles of attack and leads to a larger preload due to the aerodynamic forces and thus a larger static pitch equilibrium position. In this case no limit cycle oscillations (LCO) of the flap pitch motion induced by the freeplay gap were found. The flap pitch motions are around the upper boundary of the freeplay gap only. Buffeting flow excitation leads to a large dynamic response when the buffeting frequency is close to the flap's natural frequency.

5. Conclusions

This overview of wind tunnel model design and testing conducted at Duke University over the last twenty years has demonstrated that a standard low speed wind tunnel may be used as a test bed for a wide range of models to investigate linear and nonlinear phenomena in aeroelasticity. The data acquired have been used to validate and improve theoretical/computational models that in turn have provided a basis for high speed flow prediction of comparable phenomena. Flutter, gust response and limit cycle oscillations have been among the fundamental physical phenomena that have been studied for models with a range of nonlinear elements in the structures (including freeplay and nonlinear geometric, *i.e.*, strain-displacement relations) or aerodynamic flows (including flow separation over bluff bodies and airfoils at high angles of attack). Correlation between theory and experiment has been encouraging and has continually improved as the state of the art has progressed.

Acknowledgments: The authors would like to thank all those colleagues who have contributed to these studies over the years including the following: Peter Attar, Fanny Besem, Ping Chih Chen, Mark Connor, Chuck Denegri, Henri Gavin, Chad Gibbs, Adam Grasch, James Henry, Denis Kholodar, Bob Kielb, Dong-Hwan Lee, Daniella Raveh, Anosh Sethna, Meredith Spiker, Jeff Thomas, Steve Trickey, Lawrie Virgin, Ivan Wang, Hiroshi Yamamoto, Minghui Zhao.

Author Contributions: Deman Tang and Earl H. Dowell contributed to the aeroelastic model design, wind tunnel testing for correlation with new theory and preparation of this manuscript.

Conflicts of Interest: The authors declare no conflict of interest.

References

1. Tang, D.M.; Dowell, E.H. Experimental and Theoretical Study on Aeroelastic Response of High-Aspect Ratio Wings. *AIAA J.* **2001**, *39*, 1430–1441.
2. Tang, D.M.; Dowell, E.H. Limit Cycle Hysteresis Response for a High-Aspect Ratio Wing Model. *J. Aircr.* **2002**, *39*, 885–888.
3. Tang, D.M.; Dowell, E.H. Experimental and Theoretical Study of Gust Response for a High-Aspect Ratio Wing. *AIAA J.* **2002**, *40*, 419–429.
4. Tang, D.M.; Grasch, A.; Dowell, E.H. Gust Response for Flexibly Suspended High-Aspect Ratio Wing. *AIAA J.* **2010**, *48*, 2430–2444.
5. Tang, D.M.; Dowell, E.H. Flutter/LCO Suppression of High Aspect Ratio Wings. *J. R. Aeronaut. Soc.* **2009**, *113*, 409–416.
6. Tang, D.M.; Henry, J.K.; Dowell, E.H. Limit Cycle Oscillations of Delta Wing Models in Low Subsonic Flow. *AIAA J.* **1999**, *37*, 1355–1362.
7. Tang, D.M.; Dowell, E.H. Effects of Angle of Attack on Nonlinear Flutter of a Delta Wing. *AIAA J.* **2001**, *39*, 15–21.
8. Tang, D.M.; Attar, P. J.; Dowell, E.H. Flutter/LCO Analysis and Experiment for a Wing-Store Model. *AIAA J.* **2006**, *44*, 1662–1675.
9. Tang, D.M.; Dowell, E.H. Flutter and Limit Cycle Oscillations for a Wing-Store Model with Freeplay. *J. Aircr.* **2006**, *43*, 487–503.
10. Attar, P. J.; Dowell, E.H.; Tang, D.M. Modeling the LCO of a Delta Wing Model with an External Store Using a High Fidelity Structural Model. In Proceedings of the AIAA SDM Conference, Austin, Texas, 18–21 April 2005.
11. Tang, D.M.; Yamamoto, H.; Dowell, E.H. Experimental and Theoretical Study on Limit Cycle Oscillations of Two-Dimensional Panels in Axial Flow . *J. Fluids Struct.* **2003**, *17*, 225–242.
12. Gibbs, C.; Sethna, A.; Wang, I.; Tang, D.M.; Dowell, E.H. Aeroelastic Stability of a Cantilevered Plate in Yawed Subsonic Flow. *J. Fluids Struct.* **2014**, *49*, 450–462.
13. Tang, D.M.; Gibbs, C.; Dowell, E.H. Nonlinear Aeroelastic Analysis with Inextensible Plate Theory Including Correlation with Experiment. *AIAA J.* **2015**, *53*, 1299–1308.
14. Attar, P. J.; Dowell, E.H.; Tang, D.M. A Theoretical and Experimental Investigation of the Effects of a Steady Angle of Attack on the Nonlinear Flutter of a Delta Wing Plate Model. *J. Fluids Struct.* **2003**, *17*, 243–259.
15. Tang, D.M.; Dowell, E.H. Theoretical and Experimental Aeroelastic Study for Folding Wing Structures. *J. Aircr.* **2008**, *45*, 1136–1147.

16. Peter, J.A.; Tang, D.M.; Dowell, E.H. Nonlinear Aeroelastic Study for Folding Wing Structures. *AIAA J.* **2010**, *48*, 2187–2195.
17. Tang, D.M.; Henry, J.K.; Dowell, E.H. Nonlinear Aeroelastic Response of a Delta Wing to Periodic Gust. *J. Aircr.* **2000**, *37*, 155–164.
18. Tang, D.M.; Henry, J.K.; Dowell, E.H. Effects of Steady Angle of Attack on Nonlinear Gust Response of a Delta Wing Model. *J. Fluids Struct.* **2002**, *16*, 1093–1110.
19. Tang, D.M.; Dowell, E.H. Experimental and Theoretical Study of Gust Response for a Wing-Store Model with Freeplay. *J. Sound Vib.* **2006**, *295*, 659–684.
20. Conner, M.C.; Tang, D.M.; Dowell, E.H.; Virgin, L.N. Nonlinear Behavior of a Typical Airfoil Section with Control Surface Freeplay: A Numerical and Experimental Study. *J. Fluids Struct.* **1997**, *11*, 89–112.
21. Tang, D.M.; Dowell, E.H.; Virgin, L.N. Limit Cycle Behavior of an Airfoil with a Control Surface. *J. Fluids Struct.* **1998**, *12*, 839–858.
22. Tang, D.M.; Kholodar, D.; Dowell, E.H. Nonlinear Aeroelastic Response of a Typical Airfoil Section with Control Surface Freeplay. In Proceedings of the 41st Structures, Structural Dynamics, and Materials Conference and Exhibit, AIAA 2000-1621, Atlanta, GA, USA, 3–6 April 2000.
23. Tang, D.M.; Dowell, E.H. Aeroelastic Airfoil with Free Play at Angle of Attack with Gust Excition. *AIAA J.* **2010**, *48*, 427–442,
24. Tang, D.M.; Gavin, H.P.; Dowell, E.H. Study of Airfoil Gust Response Alleviation Using an Electro-Magnetic Dry Friction Damper–Part 2: Experiment. *J. Sound Vib.* **2004**, *267*, 875–897.
25. Lee, D.-H.; Chen, P.C.; Tang, D.M.; Dowell, E.H. Nonlinear Gust Response of a Control Surface with Freeplay. In Proceedings of the 51st AIAA/ASME/AHS/ASC Structures, Structural Dynamics and Materials Conference, AIAA 2010-3116, Oriando, FL, USA, 12–15 April 2010.
26. Tang, D.M.; Dowell, E.H. Aeroelastic Response Induced by Freeplay: Part II, Theoretical/Experimental Correlation Analysis. *AIAA J.* **2011**, *49*, 2543–2554.
27. Tang, D.M.; Dowell, E.H. Computational/Experimental Aeroelastic Study For A Horizontal Tail Model with Freeplay. *AIAA J.* **2013**, *51*, 341–352.
28. Tang, D.M.; Dowell, E.H. Effects of a Free-to-Roll Fuselage On Wing Flutter: Theory and Experiment. *AIAA J.* **2014**, *52*, 2625–2632.
29. Tang, D.M.; Dowell, E.H. Experimental Aerodynamic Response for an Oscillating Airfoil in Buffeting Flow. *AIAA J.* **2014**, *52*, 1170–1179.
30. Tang, D.M.; Dowell, E.H. Experimental Aeroelastic Response for a Freeplay Control Surface in Buffeting Flow. *AIAA J.* **2013**, *51*, 2852–2861.
31. Hodges, D.H.; Dowell, E.H. *Nonlinear Equations of Motion for the Elastic Bending and Torsion of Twisted Nonuniform Rotor Blades*, Technical Report NASA TN D-7818; NASA: Washington, DC, USA, 1974.
32. Tran, C.T.; Petot, D. Semi-Empirical Model for the Dynamic Stall of Airfoils in View to the Application to the Calculation of Responses of a Helicopter Blade in Forward Flight. *Vertica* **1981**, *5*, 35–53.
33. Simmonds, J.G.; Libal, A. Exact equations for the inextensional deformation of cantilevered plates. *J. Appl. Mech.* **1979**, *46*, 631–636.
34. Simmonds, J.G.; Libal, A. Alternate exact equations for the inextensional deformation of arbitrary, quadrilateral, and triangular plates. *J. Appl. Mech.* **1979**, *46*, 895–900.
35. Simmonds, J.G. Exact equations for the large inextensional motion of plates. *J. Appl. Mech.* **1981**, *48*, 109–112.
36. Darmon, P.; Benson, R.G. Numerical Solution to an Inextensible Plate Theory with Experimental Results. *J. Appl. Mech.* **1986**, *53*, 886-890.
37. Tang, D.M.; Zhao, M.; Dowell, E.H. Inextensible Beam and Plate Theory: Computational Analysis and Comparison with Experiment. *J. Appl. Mech.* **2014**, *81*, doi:10.1115/1.4026800.
38. Molyneux, W.G. *The Flutter of Swept and Unswept Wing with Fixed-Root Conditions*; HM Stationery Office: London, UK, 1950.
39. Yates, E.C., Jr. *AGARD Standard Aeroelastic Configurations for Dynamic Response I—Wing 445.6*, NASA-TM-100492; NASA Langley Research Center: Hampton, VA, USA, 1 August 1987.
40. Weatin, M.F.; Goes, L.C.; Ramos, R.L.; Silva, R.G. Aeroservoelastic Modeling of a Flexible Wing for Wind Tunnel Flutter Test. In Proceedings of 20th International Congress of Mechanical Engineering (p.9), Gramado, RS, Brasil, 15–20 November 2009.

41. Edwards, J.W.; Schuster, D.M.; Spain, C.V.; Keller, D.F.; Moses, R.M. MAVRIC Flutter Model Transonic Limit Cycle Oscillation Test. In Proceeding of the 19th AIAA Applied Aerodynamics Conference, AIAA-2001-1291, Anaheim, CA, USA, 16–19 April 2001.
42. Peters, D.A.; Cao, W.M. Finite State Induced Flow Models, Part I: Two-Dimensional Thin Airfoil. *J. Aircr.* **1995**, *32*, 313–322.
43. Niles, R.H.; Spielberg, I.N. *Subsonic Flutter Tests of an Unswept All-Movable Horizontal Tail,* WADC TR-54-53, AD 39949; Wright Air Development Center Wright-Patterson AFB: Dayton, OH, USA, March 1954.
44. Niles, R.H. *Subsonic Flutter Model Tests of an All-Movable Stabilizer with 35° Sweepback*, WADC Technical Note 55-623, AD 91593; Wright Air Development Center Wright-Patterson AFB: Dayton, OH, USA, November 1955.
45. Cooley, D.E.; Murphy, J.A. *Subsonic Flutter Model Tests of a Low Aspect Ratio Unswept All-Movable Tail*, WADC-TR-58-31, AD 142337; Wright Air Development Center Wright-Patterson AFB: Dayton, OH, USA, February 1958.
46. Raveh, D.E. Numerical Study of an Oscillating Airfoil in Transonic Buffeting Flows. *AIAA J.* **2009**, *47*, 505–515.
47. Raveh, D.E.; Dowell, E.H. Frequency Lock-in Phenomenon for Oscillating Airfoils in Buffeting Flows *J. Fluids Struct.* **2011**, *27*, 89–104.
48. Dowell, E.H.; Hall, K.C.; Thomas, J.P.; Kielb, R.E.; Spiker, M.A.;Denegri, C.M., Jr. A New Solution Method for Unsteady Flows Around Oscillating Bluff Bodies. In IUTAM Symposium on Fluid-Structure Interaction in Ocean Engineering, Proceedings of the IUTAM Symposium, Hamburg, Germany, 23–26 July 2007; Springer: New York, NY, USA, p. 37.
49. Chen, J.; Fang, Y.C. Lock-on of Vortex Shedding due to Rotational Oscillations of a Flat Plane in a Uniform Stream. *J. Fluid Struct.* **1997**, *12*, 779–798.
50. Hall, K.C.; Thomas, J.P.; Clark, W.S. Computation of Unsteady Nonlinear Flows in Cascades Using a Harmonic Balance Technique. *AIAA J.* **2002**, *40*, 879–886.
51. Besem, F.; Kamrass, J.D.; Thomas, J.P.; Tang, D.M.; Kielb, R.E. Vortex-Induced Vibration and Frequency Lock-in of An Airfoil at High Angles of Attack. *J. Fluids Eng. Trans. ASME* **2016**, *138*, doi:10.1115/GT2014-25648.